

# Fluid-Structure Interaction Simulations of Rocket Engine Side Loads

Eric L. Blades<sup>1</sup>, Mary Baker<sup>1</sup>, Carl L. Pray<sup>1</sup>, and Edward A. Luke<sup>2</sup>

<sup>1</sup>ATA Engineering, Inc., San Diego, CA 92130

<sup>2</sup>Mississippi State University, Starkville, MS 39762

*Abstract: The goal of this work was to simulate both the flow in a rocket engine nozzle and the resulting flow-induced transient loads on the nozzle. This unsteady nozzle flow results in structural dynamic excitation, which contributes not only to nozzle stress and deformation but also to the dynamic loads that are transmitted to the rest of the engine. This paper demonstrates the capability of a coupled fluid-structure interaction (FSI) simulation for predicting side loads on a rocket engine nozzle. The capability was demonstrated using the space shuttle main engine (SSME) during a portion of the engine startup sequence. A comparison to the rigid nozzle baseline solution was made, and the FSI solutions demonstrate the effect of nozzle flexibility on the structural and fluid dynamic response. Abaqus/Standard was used to compute the unsteady structural responses, and the Loci/CHEM CFD program was used to simulate the unsteady, separated flow in the nozzle. The FSI simulations were performed using the Co-Simulation Engine (CSE) to couple the unsteady fluid and structural responses. Multiple fluid and structural cases were explored to achieve realistic and qualitatively correct flow and structural responses in preparation for the coupled solution attempts. These unsteady FSI results represent the first fully coupled, time-accurate, viscous FSI simulation for a rocket engine nozzle.*

*Keywords: Computational Fluid Dynamics, Coupled Analysis, Co-Simulation Engine, Fluid-Structure Interaction, Flow Separation, Liquid Rocket Engine, Nozzle Side Loads*

## 1. Introduction

Next-generation launch systems will require propulsion systems that deliver high thrust-to-weight ratios, increased trajectory-averaged specific impulse, reliable overall vehicle systems performance, low recurring costs, and other innovations to achieve cost and crew safety goals.

To minimize risk, these programs have typically made only incremental improvements, since they utilized heritage designs or otherwise had to be very conservative in their design approach. These strategies have resulted in heavier engines, with the engine sometimes accounting for a significant portion of the launch vehicle mass fraction. One of the main barriers to innovation and lighter-weight components has been uncertainty in the loads definition. Load determination challenges include simulating the interaction of many components, addressing many different loading conditions, and determining the combined effect of different types of loads.

Recent advances in computer power as well as in analysis techniques such as finite element analysis (FEA) and computational fluid dynamics (CFD) have made more-realistic loads simulations feasible within the design process. Yet the lack of validation of these methods in previous hardware programs or against test data has been a barrier to implementing them at a level that can enable the faster definition of more-innovative, higher-performing propulsion systems at significantly reduced weight while maintaining acceptable levels of risk.

The dynamic loads that a rocket engine endures can be broadly categorized into boost-induced (e.g., first-stage launch loads on a second-stage engine) and self-induced loads. The self-induced loads can further be categorized into mechanical and flow-induced loads. In order to define the structure of each engine component, all of these loads need to be simulated or estimated and combined in the component design loads and then used to define margins and predict life for that component.

### **1.1 Flow Separation in Nozzles**

Figure 1 shows Mach number contours from an SSME transient startup simulation in an overexpanded operating condition. A shock-wave system is formed in the nozzle due to the supersonic flow encountering the adverse pressure gradient in the nozzle. The flow separates when the turbulent boundary layer cannot negotiate the adverse pressure gradient imposed upon it by the outer flow.

Figure 1 demonstrates both modes in which the flow can separate. The upper half of the figure illustrates a free shock separation (FSS) structure, and the lower half illustrates a restricted shock separation (RSS) structure. In the FSS mode, the flow separates from the wall and continues as a free stream. Since the SSME is a thrust-optimized/parabolic nozzle, an internal shock forms due to the curvature discontinuity where the wall contour transitions from a circular arc contour to a parabolic contour. As the chamber pressure increases, the internal shock interacts with the Mach disk (the normal shock identified in Figure 1), causing the annular supersonic plume to deflect outward and reattach to the nozzle wall. This reattachment creates a local recirculation region that is restricted in location between the separation location and the reattachment location. The transition from FSS to RSS creates a significant side load. As the chamber pressure increases further, the RSS reattachment location moves further downstream, closer to the end of the nozzle. As it approaches the nozzle exit plane, the plume oscillates between FSS and RSS, creating additional side loads.

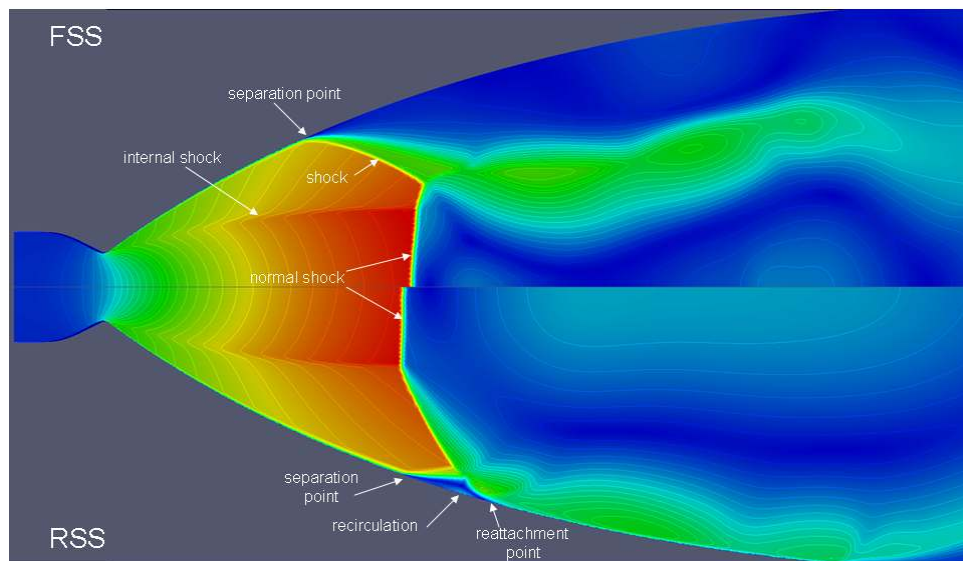


**Figure 1. Mach number contours from SSME simulation comparing free shock separation (upper) and restricted shock separation (lower).**

## 1.2 Nozzle Side Loads

Nozzle side loads occur due to asymmetry in the flow separation that is a result of the external pressure being higher than internal pressures. During the startup and shutdown of engines, the rocket nozzle is operating in an overexpanded mode where the ambient pressure is greater than the internal wall pressure acting over some portion of the nozzle. Based on test measurements, flow separation occurs when the ratio of the internal wall pressure to atmospheric pressure is in the range  $\frac{1}{4} \leq \frac{P_{wall}}{P_{atm}} \leq \frac{1}{2}$  (Nave, 1973). Due to instabilities inherent in the shock-boundary layer

interaction, the flow separation does not occur symmetrically around the nozzle but instead flaps asymmetrically. The asymmetric separation can lead to a sudden asymmetric pressure distribution in the nozzle, which results in a large-magnitude transient side load that has been known to fail the nozzle or to create a design-driving shock transient on other engine components. This pressure shock can couple to the nozzle two-nodal-diameter mode in a way that increases the severity of the impact on the engine. For example, the side loads experienced by the Japanese LE-7A engine were severe enough to cause the engine actuator to fail and to break the regenerative cooling tubes, ultimately forcing the abandonment of the film cooling design because it caused a jump in the nozzle separation line that resulted in the highest design loads (Watanabe, 2002). High side loads

also resulted in the failure of the gimbal block retaining bolts for the J-2 engine (Shi, 2005). The J-2X engine, which is currently under development as an upper-stage engine for NASA's next heavy-lift launch vehicle, is a derivative of the J-2 engine and will likely experience side loads similar to its predecessors, the J-2 and J-2S. Thus, accurate prediction of nozzle side loads is of great interest for current and future nozzle designs.

Considerable effort has been expended on better understanding these side loads with the goal of creating predictive tools that can be used to characterize the shock load such that realistic but not overly conservative loads can be used in the design. Pratt & Whitney Rocketdyne has developed a practical but conservative approach based on semi-empirical methods (Shi, 2005). NASA has embarked on a multi-year effort to develop computational and test capabilities to characterize nozzle side loads in an effort to increase the experience and knowledge base needed to support liquid rocket nozzle development (Brown, 2002, 2007, 2009; Ruf, 2009, 2010; Smalley, 2007; Wang, 2009, 2010). However, none of the computational studies incorporate nozzle flexibility coupled with CFD. Variations in the wall pressure may cause a significant distortion of the nozzle, which results in significant amplification of the initial load due to the fluid-structure coupling. This fluid-structure interaction model takes into account the influence of the nozzle deflection on the flow behavior and the subsequent effect on the wall pressure. Recent efforts by Wang et al. have attempted to characterize the effects of nozzle deformation on the separation location and subsequent side loads by performing simulations using rigid, out-of-round (oval-shaped) nozzles (Wang, 2010). The results show that the effect of nozzle deformation is important, as the peak side loads increased as the degree of out-of-roundness increased.

## **2. Technical Approach**

For the nozzle FSI simulations, a domain-decomposition approach was utilized in which the CHEM CFD solver was used to compute the nozzle flow field and forces acting on the nozzle wall, and the Abaqus nonlinear computational structural dynamics solver was used to compute the nozzle deflections. Loci/CHEM is a Reynolds-averaged Navier-Stokes finite-volume flow solver for arbitrary polyhedra developed by Dr. Edward Luke at Mississippi State University (MSU) (Luke, 2005, 2007). CHEM uses density-based algorithms and employs high-resolution approximate Riemann solvers to solve finite-rate, chemically reacting viscous turbulent flows. The coupling between the CHEM and Abaqus is accomplished using SIMULIA's Co-Simulation Engine (CSE). The data transfer at the wetted surface interface is performed using the mapping

tools provided by the CSE. Once the CFD interface or wetted surface is moved to conform to the structural deformations, the flow solver adapts the volume mesh to reflect these changes (Luke, 2012).

### **3. Development of Computational Models**

The SSME engine was selected for computational studies because there is a great wealth of information available in the form of animated pictures of startup and testing as well as many engine tests. Not only is the fluid-structure interaction clearly visible in the films of the startup transients but the resulting shock load delivered to the equipment attached to nozzle of the SSME is well documented in historical design challenges from the SSME development program. On two occasions in 1979 during the SSME development hot-firing testing, a liquid hydrogen feedline support, called the steerhorn due to its shape, failed during the cutoff transient. These failures were caused by the shock load resulting from flow separation (Larson, 1982). Observations from these failures and from scale-model testing determined that these shock loads involved the coupling of the flow separation with the nozzle two-nodal-diameter mode structural deformations. Thus these failures that resulted in hydrogen explosions were attributed to high asymmetric side loads that would require fluid-structure interaction to simulate. These phenomena motivated the use of the SSME as the computational test article in the development of simulation tools that are being developed to prevent this type of failure in future engine programs.

#### **3.1 Structural Models**

A finite element model of the SSME was constructed. The FEM included the nozzle, throat, hat band stiffeners, gimbal, and actuators. Modal data was used to correlate the first three nodal diameters (N=2,3,4) of the FEM, as shown in Figure 2.

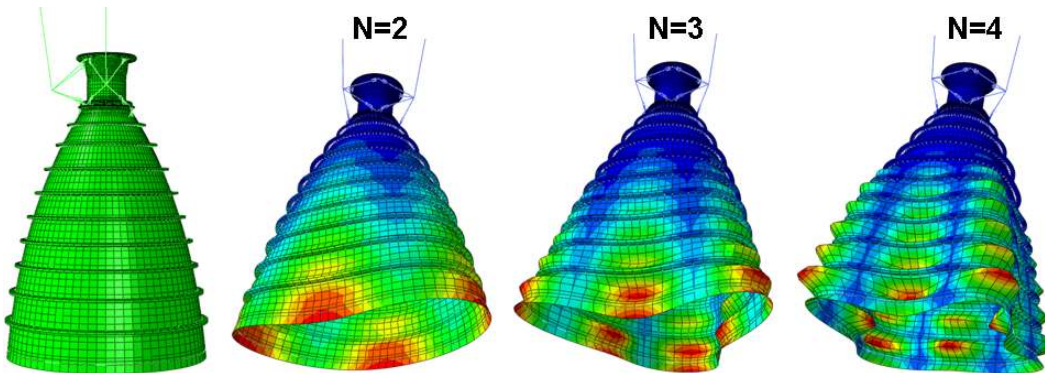


**Figure 2. Finite element model and the first three nodal diameter modes.**

The structural model nozzle properties resulted in local panel modes in the nozzle between the hat band stiffeners. These local panel modes were thought to cause problems in the FSI simulations, so a simplified model was created that removed the hat bands and used smoothed nozzle properties to model the stiffness of the nozzle tubes and hat bands. The smoothed nozzle properties increased the frequency of the nozzle panel modes, essentially eliminating this type of mode at low frequencies.

For the smoothed nozzle, the anisotropic material properties were converted to isotropic materials. A constant elastic modulus was first used to match the experimentally determined N=3 and N=4 modes. A Young's modulus of  $3.6 \times 10^{12}$  psi gave the best match to these modes. The properties of the mid-span of the nozzle were then adjusted to match the N=2 mode more closely. The nozzle forward-end properties were adjusted to match the throat bending mode. The density remained the same to keep the mass consistent.

### **3.2 Computational Fluid Dynamics Models**

Using the SSME nozzle profile for the SSME block II, large throat configuration, the computational domain for the CFD mesh, including the far field boundaries, was constructed. The outflow boundary is 32 nozzle exit radii ( $R_E$ ) downstream of the nozzle exit plane, and the outer far field boundary is located approximately  $7R_E$  above the centerline.

The three-dimensional nozzle mesh was created in two pieces by revolving a two-dimensional mesh, meshing the centerline region separately, and finally merging the two meshes to create the final volume mesh. The first piece of the volume mesh was constructed by revolving the two-dimensional mesh in  $6^\circ$  increments, resulting in a volume mesh containing 9.3 M cells and having

a circumferential resolution of 60 elements. However, to avoid numerical problems with elements along the centerline, the centerline was offset radially inward, leaving a cylindrical hole along the centerline of the revolved 3-D mesh. To mesh this cylindrical region, the surface mesh of the cylindrical hole was extracted from the revolved volume mesh, and circular surface meshes were merged at both ends of the cylinder to create a closed surface mesh. This surface mesh was used to generate a cylindrical volume mesh containing 3.1 M cells using the structured-layer meshing capability in the AFLR3 mesh generator. The revolved mesh and cylindrical mesh were then merged to create the final, three-dimensional, full-annulus, unstructured, viscous volume mesh of the SSME nozzle, containing 12.34 M cells.

The inlet and outer boundaries used inflow-type boundary conditions to specify standard sea-level conditions with a very small inflow velocity. The exit boundary was set to an outflow boundary with a slightly lower value of static pressure to ensure that the far field flow exits the domain. An inflow boundary condition was applied at the combustion chamber inlet boundary to represent the chamber “plenum” conditions. The nozzle and combustion chamber walls used a no-slip boundary condition with the prescribed temperature distribution. For all the results presented here, the working fluid is a single-species perfect gas with properties designed to be representative of the SSME exhaust gas.

## **4. Coupled Fluid-Structural Simulations**

Fully coupled, time-accurate, viscous FSI simulations of the SSME were performed and the results were compared to a rigid nozzle solution. No structural damping is assumed in any of the FSI simulations. In addition to the fluid dynamic load applied to the nozzle, a uniform pressure loading corresponding to one atmosphere was applied.

### **4.1 Rigid Nozzle Simulation**

A time-accurate simulation performed using a rigid nozzle was run for approximately 0.02 seconds using a time step of  $2 \times 10^{-6}$  seconds. The initial conditions correspond to a nozzle pressure ratio of approximately 59. At these conditions, the flow is in the FSS state, the separation point is approximately 51 inches downstream of the throat, and the flow exhibits oscillatory behavior due to asymmetric flow separation and results in side forces of approximately 40,000 Newtons.

## 4.2 Quasi-Static Fluid-Structure Interaction Simulation

For the FSI simulations, rather than start immediately from the rigid-nozzle initial conditions at  $t=0.79$  sec, it was thought better to start from a static aeroelastic or quasi-steady equilibrium condition. Doing so avoided an impulsive start and the excitation of high-frequency structural modes and also allowed the structure to respond more slowly to the aerodynamic forces being applied. A quasi-steady aeroelastic solution was obtained by using the Abaqus/Standard static solver and running CHEM in a “steady-state” mode.

The coupled quasi-steady FSI simulation was run for 5,500 iterations; the integrated forces acting on the diverging section of the nozzle are shown in Figure 3. After 5,550 iterations, the response undergoes  $4\frac{1}{2}$  cycles and the lateral forces appear to remain nearly periodic and exhibit very small amounts of damping. The displacement of a node (Node 3) on the trailing edge of the nozzle is shown in Figure 4. In the figure, the displacement response is exhibiting similar behavior to the integrated force response. Since the solution does not appear to be converging to an equilibrium position, the question becomes which quasi-steady solution should be used as the starting condition for the unsteady FSI simulations. In Figure 5, the vertical component of the integrated force and the vertical component of displacement of Node 3 are plotted together; note that the displacement is scaled by  $1 \times 10^6$  so that it can be viewed on the same scale as the force. After approximately 500 iterations, the structural response appears to have adjusted to the fluid dynamics, and this point was chosen as the restart solution for the unsteady FSI simulations. The deformed nozzle at this state is shown in Figure 6, and the magnitude of the maximum deflection is 0.02858 m (1.125 in).



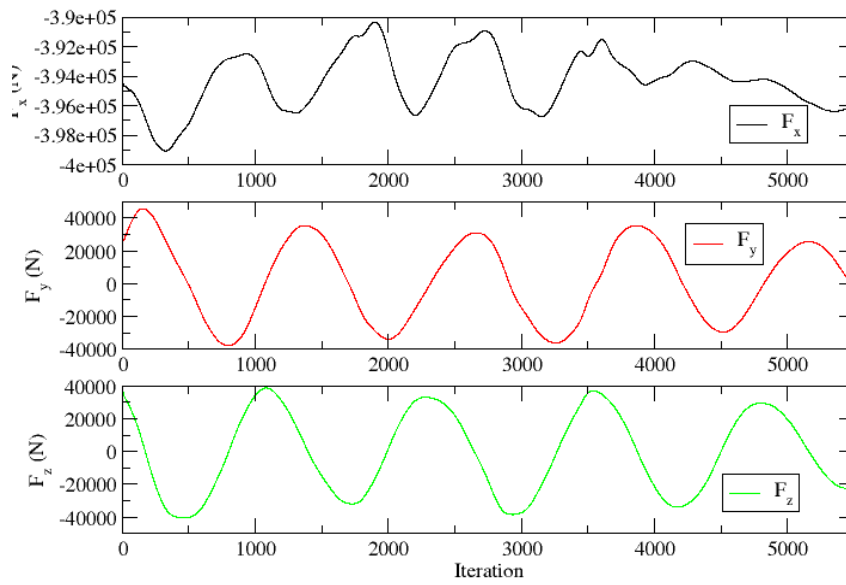


**Figure 3. Quasi-steady forces on the diverging section of the nozzle in the (a) X direction, (b) Y direction, and (c) Z direction.**

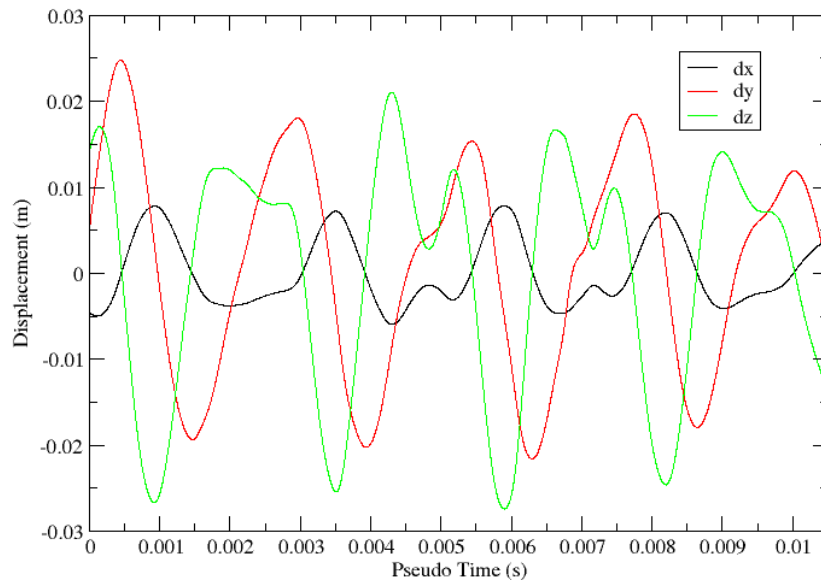


**Figure 4. Quasi-steady displacement response for a node on the trailing edge of the nozzle.**

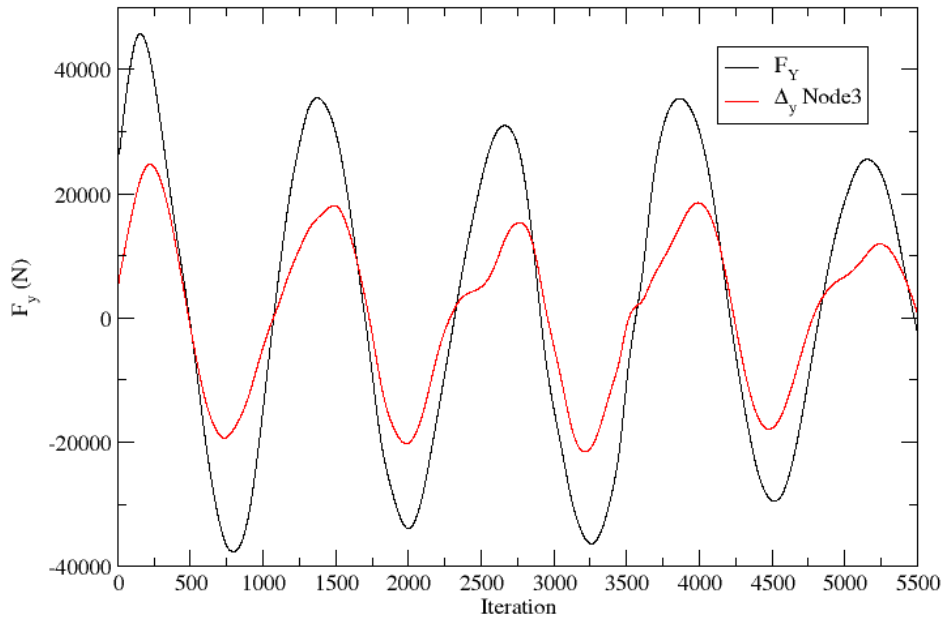


**Figure 5. Quasi-steady force and displacement response (note that displacement response is scaled by  $1 \times 10^6$ ).**

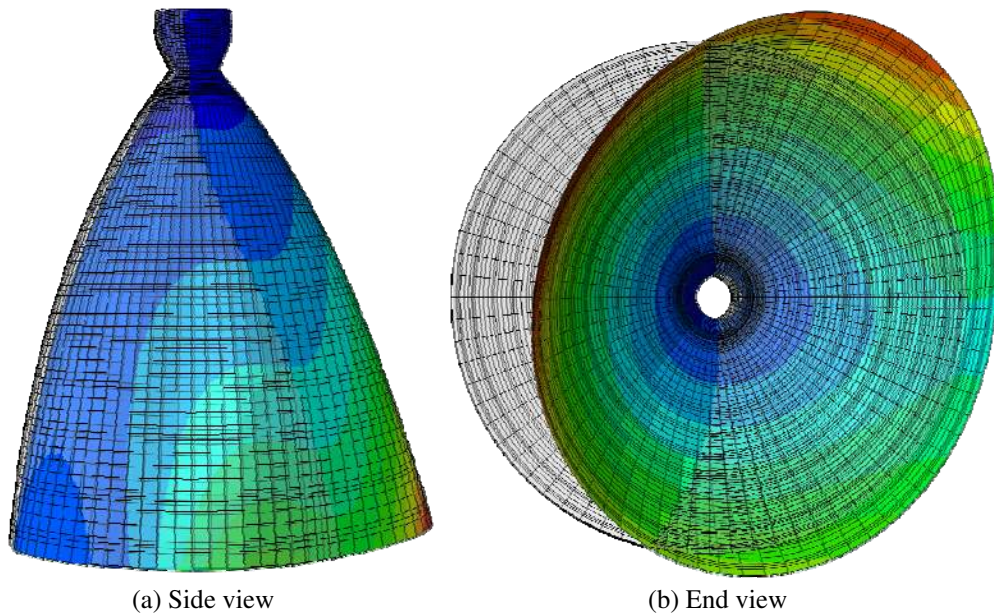
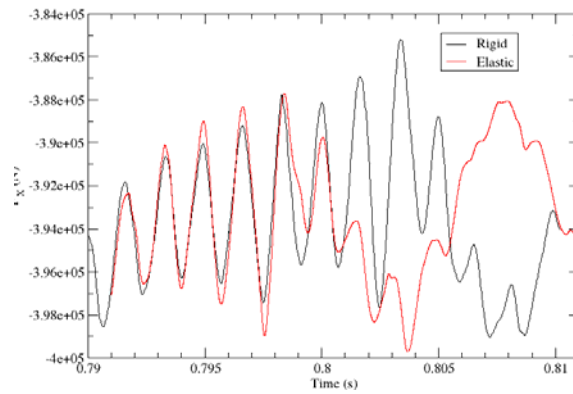


**Figure 6. Quasi-steady deformation of the nozzle after 500 iterations.**

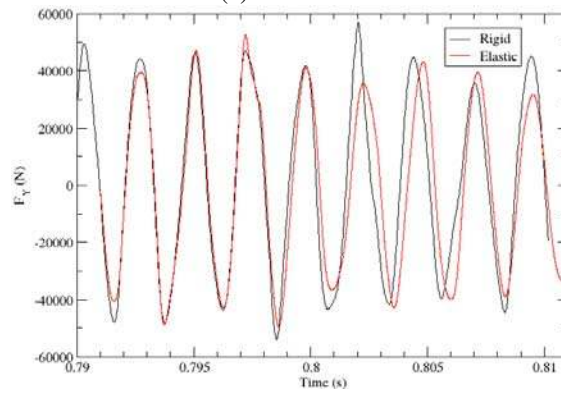
### 4.3 Unsteady Fluid-Structure Interaction Simulations

After approximately 500 iterations, the structural response appeared to have adjusted to the fluid dynamics, and the solution was restarted for the unsteady FSI simulations. A comparison of the unsteady integrated force on the diverging section of the nozzle is shown in Figure 7. The X-direction force for the elastic nozzle results in slightly higher thrust loads compared to the rigid nozzle during the first 0.01 seconds, and the force for the elastic nozzle has the same frequency of approximately 600 Hz. However, over the last 0.01 seconds, the axial force for the elastic nozzle is out of phase compared to the rigid nozzle. For the vertical or Y-direction force, the extreme value of the forces for the elastic nozzle differs by approximately 5% in the first 0.01 seconds and elastic nozzle forces have the same frequency of oscillation as those of the rigid solution: 400 Hz. In the last 0.01 seconds, the elastic nozzle tends to reduce the peak values and lower the frequency of the vertical component of the side load. The frequency coincides with a change in separation location for the elastic nozzle, as illustrated in Figure 8. The lateral or Z-direction force for the elastic nozzle exhibits the same trends as the vertical force. Compared to the rigid nozzle lateral force, the elastic nozzle lateral force has the same frequency of oscillation during the first 0.01 seconds and then a lower frequency in the last 0.01 seconds.

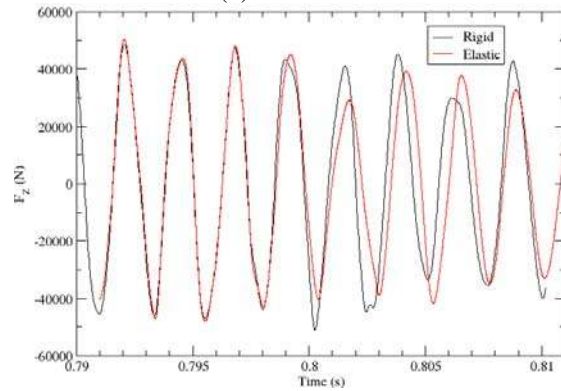
The instantaneous pressure distribution along the nozzle centerline, plotted for two different time instances, is shown in Figure 8. The pressure distributions for the upper surface are colored black (rigid nozzle) and red (elastic nozzle) and those for the lower surface are green (rigid nozzle) and blue (elastic nozzle). Also included is an inset of the lateral force (Y-direction) time history comparison (black/rigid and red/elastic) with a green time-indicator bar. Note that the ratio of the wall pressure to the atmospheric pressure is 0.25 and that this is in the range where the nozzle flow separation occurs randomly (Shi, 2005) In Figure 8 (a) and (b), the separation location for the rigid and elastic nozzle is the same, and the frequency of the lateral force coincides as well. The flow asymmetry is evident in the difference in separation location between the upper surface (red/black) and the lower surface (blue/green). The oscillatory nature of the lateral force is due to the change in separation location as demonstrated in Figure 8 (a)–(f). As the solution evolves over time, there is a shift in the frequency of the lateral force as indicated in Figure 8 (c)–(f). This shift in frequency coincides with the change in separation location for the elastic nozzle as evident in the difference of the predicted separation location between black and red curves and between the green and blue curves. It is this oscillating force effect on the nozzle nodal diameter modes that is of particular interest in determining nozzle and engine loads.



(a) X direction



(b) Y direction



(c) Z direction

**Figure 7. Comparison of the integrated force on the downstream portion of the nozzle using the simplified FEM showing significant differences in forces, particularly in the axial direction.**

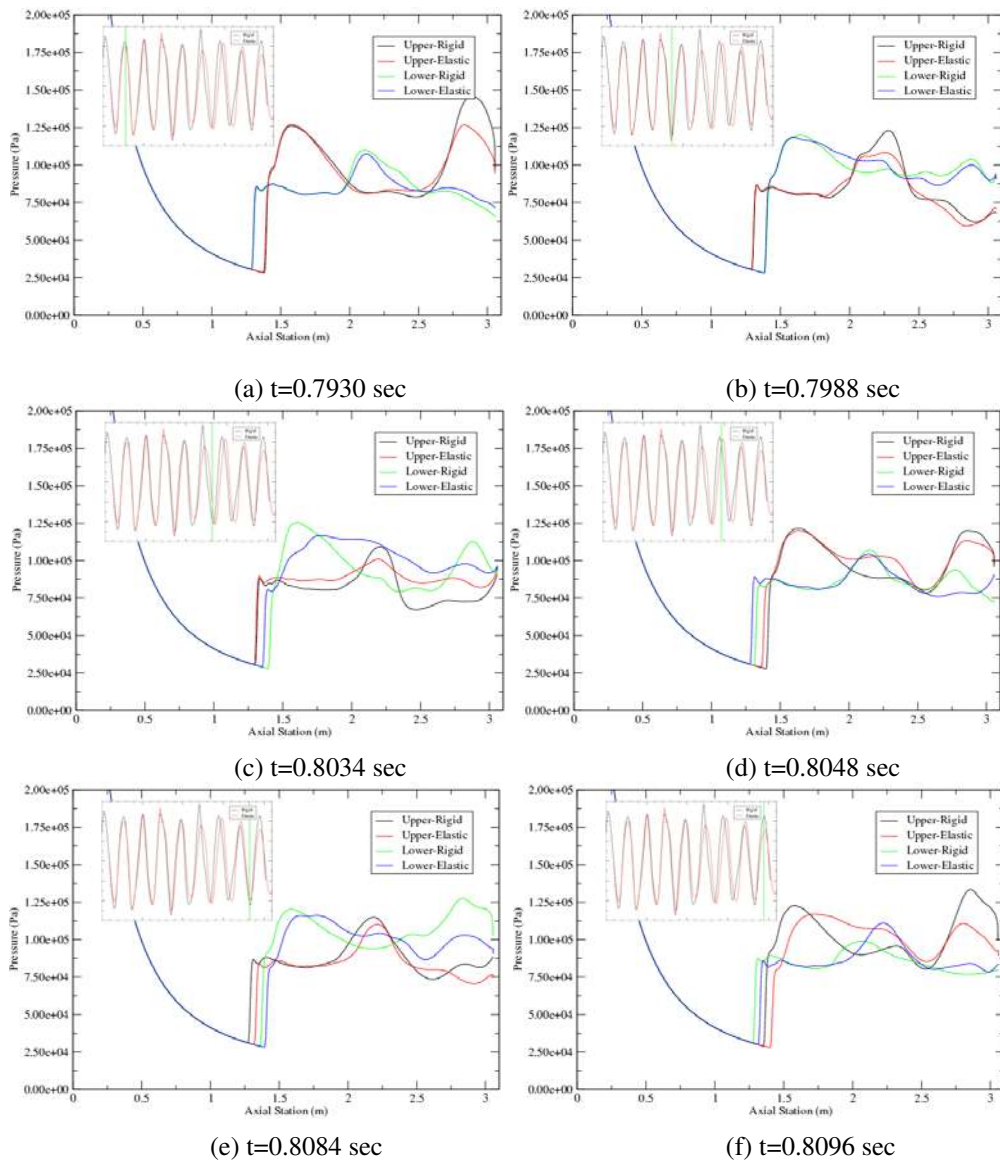


**Figure 8. Comparison of nozzle centerline instantaneous wall pressure distributions.**

The displacement of the nozzle at various time steps is shown in Figure 9 and Figure 10; it is not symmetric. The maximum total displacement over the time interval occurs at the trailing edge of the nozzle and is approximately 1.13 inches. The overall deflection of the nozzle is governed

predominantly by the pendulum and second nodal diameter modes of the nozzle, which for the smoothed FEM are approximately 22.7 and 26.8 Hz. The deflection of node 3, shown in Figure 11, illustrates the predominant low-frequency response of the nozzle at around 25 Hz. Figure 12 shows the displacement time history of four points on the nozzle trailing edge that are spaced approximately 90° apart. The asymmetric deformation of the nozzle is further evident from the fact that displacement curves for each node do not all intersect at the same point. The displacement of each node consists of a low-frequency response at approximately 25–30 Hz and a high-frequency response superimposed at approximately 400 Hz. The high-frequency response is most noticeable in the vertical or Y-direction response as illustrated in Figure 12(b). The high-frequency response corresponds to the frequency of the vertical and lateral force oscillations. The low-frequency structural response correlates well to the N=2 mode, which is consistent with physical observations on the SSME during testing and operation.

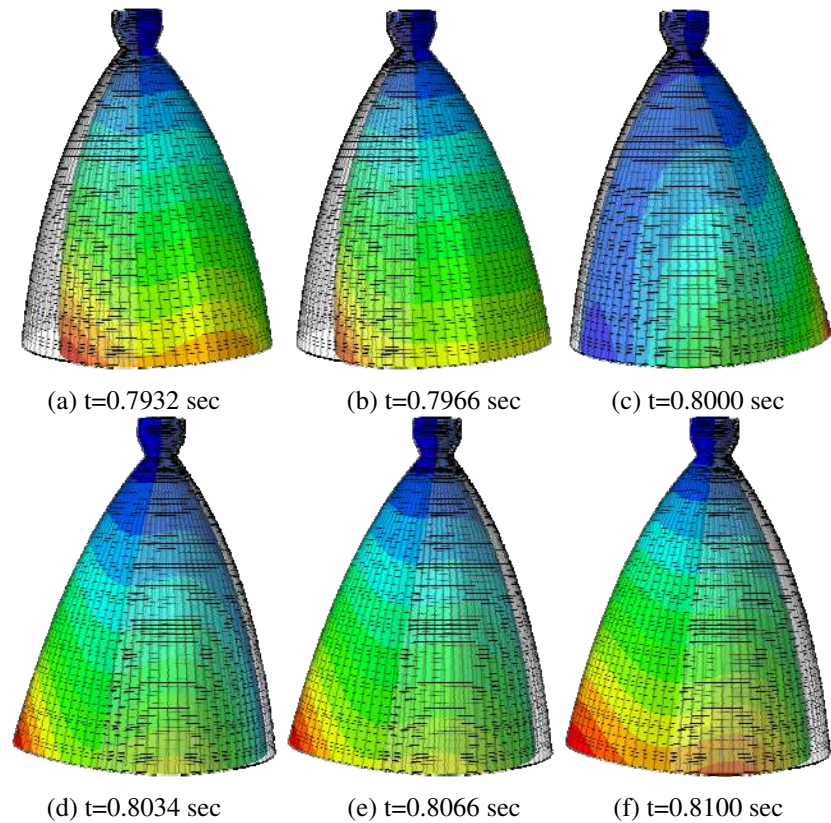


**Figure 9. Nozzle deformed shape and deformation contours: side view.**



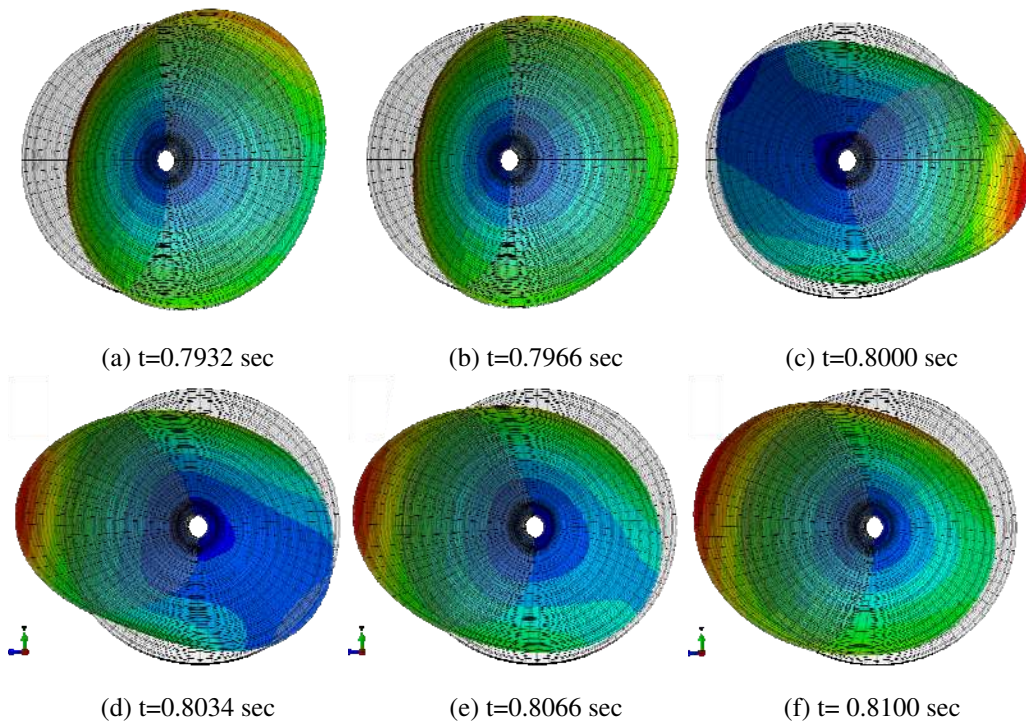


**Figure 10. Nozzle deformed shape and deformation contours: end view.**

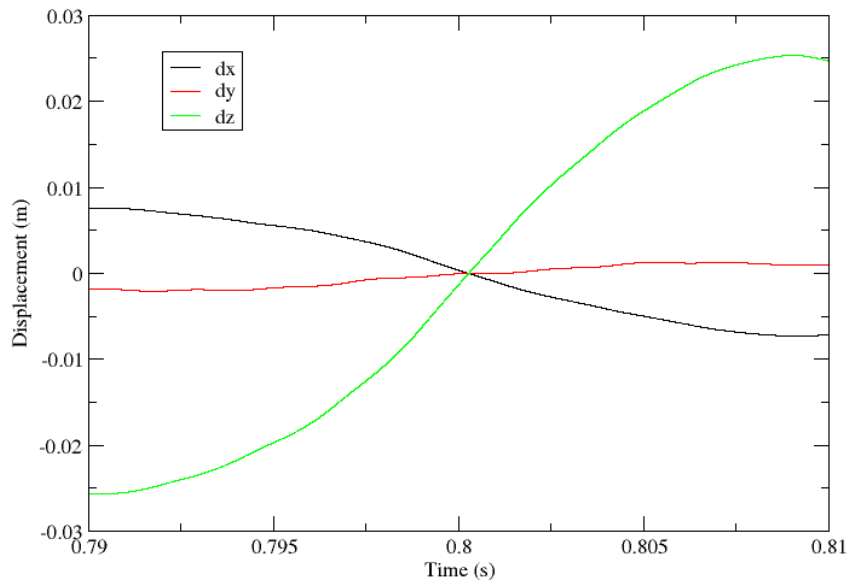
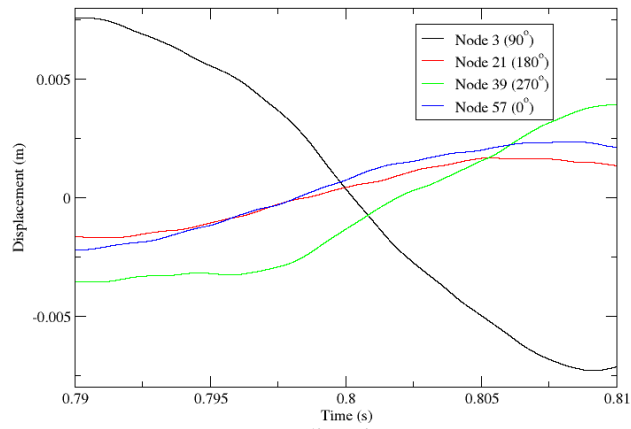
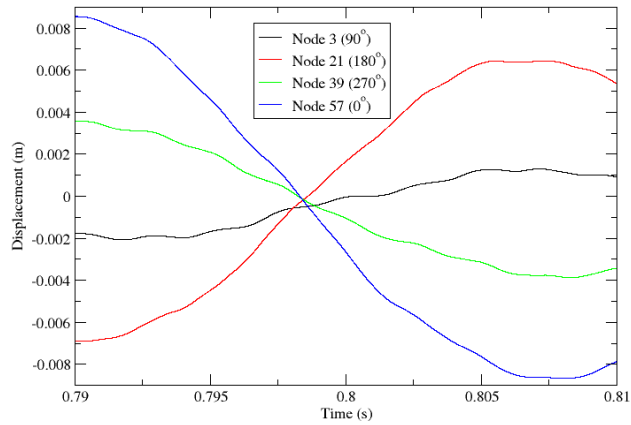


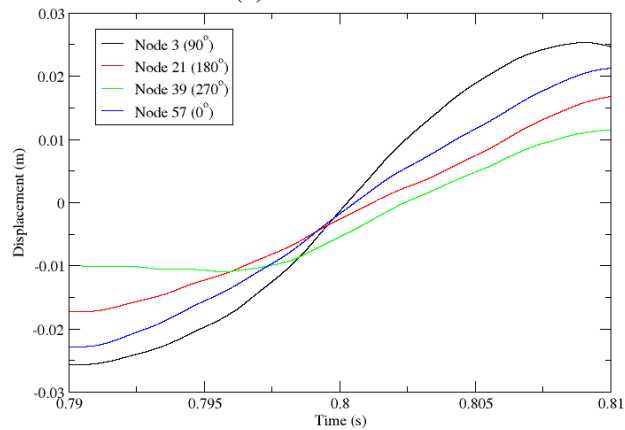
**Figure 11. Displacement time history for Node 3.**



(a) X direction



(b) Y direction



(c) Z direction

Figure 12. Displacement of nodes along the trailing edge of the nozzle.



The FSI solutions demonstrate the effect of nozzle flexibility on the structural and fluid dynamic response and the feasibility of the fluid-structure coupling as applied to a three-dimensional, time-accurate, viscous FSI simulation for a rocket engine nozzle.

The results for all of the simulations presented here were obtained using the high-performance computing resources at the Alabama Supercomputing Authority (ASC). All simulations were performed using 128 cores on the dense memory Linux cluster at ASC. The unsteady FSI simulations took approximately 22,000 CPU hours, compared to the rigid nozzle simulations which took approximately 11,000 CPU hours. Future efforts will focus on ways to reduce the additional computational expense of the FSI simulations.

## 5. Conclusions

A capability for a coupled fluid-structure interaction simulation using computational fluid dynamics and computational structural dynamics for predicting side loads on a rocket engine nozzle has been demonstrated. The capability was demonstrated using the space shuttle main engine during a portion of the engine startup sequence. A comparison to the rigid nozzle baseline solution was made, and the FSI solutions demonstrate the effect of nozzle flexibility on the structural and fluid dynamic response. These simulations represent the first ever fully coupled, time-accurate, three-dimensional FSI simulation of a rocket engine nozzle.

## 6. References

1. Nave, L. H., and G. A. Coffey, "Sea Level Side Loads in High-Area-Ratio Rocket Engine," AIAA-73-1283, Nov. 1973.
2. Watanabe, T., N. Sakazume, and M. Tsuboi, "LE-7A Engine Nozzle Problems During the Transient Operations," AIAA-2002-3841, July 2002.
3. Shi, J., "Rocket Engine Side Load Transient Analysis Methodology – A Practical Approach," AIAA-2005-1860, Apr. 2005.
4. Brown, A. M., J. Ruf, D. Reed, M. D'Agostino, and R. Keanini, "Characterization of Side Load Phenomena Using Measurement of Fluid/Structure Interaction," AIAA-2002-3999, July 2002.
5. Wang, T.S., "Transient Three-Dimensional Analysis of Side Load in Liquid Rocket Engine Nozzles," AIAA-2004-3681, July 2004.
6. Brown, A. M., and J. Ruf, "Calculating Nozzle Side Loads Using Acceleration Measurements of Test-Based Models," Proceedings of the 25th International Modal Analysis Conference, Feb. 2007.

7. Smalley, K. B., A. M. Brown, and J. Ruf, "Flow Separation Side Loads Excitation of Rocket Nozzle FEM," AIAA-2007-2242, Apr. 2007.
8. Brown, A. M., J. H. Ruf, and D. M. McDaniels, "Recovering Aerodynamic Side Loads on Rocket Nozzles Using Quasi-Static Strain-Gage Measurements," AIAA-2009-2681, May 2009.
9. Ruf, J. H., D. M. McDaniels, and A. M. Brown, "Nozzle Side Load Testing and Analysis at Marshall Space Flight Center," AIAA-2009-4856, Aug. 2009.
10. Wang, T. S., "Transient Three-Dimensional Startup Side Load Analysis of a Regeneratively Cooled Nozzle," *Shock Waves*, vol. 19 (2009): 251–64.
11. Wang, T. S., J. Lin, J. Ruf, and M. Guidos, "Transient Three-Dimensional Side Load Analysis of Out-of-Round Film Cooled Nozzles," AIAA-2010-6656, July 2010.
12. Ruf, J. H., D. M. McDaniels, and A. M. Brown, "Details of Side Load Test Data and Analysis for a Truncated Ideal Contour Nozzle and a Parabolic Contour Nozzle," AIAA-2010-6813, July 2010.
13. Luke, E., and T. George, "Loc: A Rule-Based Framework for Parallel Multidisciplinary Simulation Synthesis," *Journal of Functional Programming* (Cambridge University Press) vol. 15, no. 3 (2005): 477–502.
14. Luke, E., "On Robust and Accurate Arbitrary Polytope CFD Solvers (Invited)," AIAA 2007-3956, 2007.
15. Luke, E., E. Collins, and E. Blades, "A Fast Mesh Deformation Method Using Explicit Interpolation," *Journal of Computational Physics*, vol. 231, no. 2, (2012): 586–601.
16. Larson, E. W., G. H. Ratekin, and G. M. O'Connor, "Structural Response of the SSME Fuel Feedline to Unsteady Shock Oscillations Pt 2," *The Shock and Vibration Bulletin*, May 1982, 177–82.

## 7. Acknowledgements

This work was completed with SBIR funding from NASA Marshall Space Flight Center, contract NNX11CH34P, Mr. Joseph Ruf and Dr. Andrew Brown, program managers. The authors would like to acknowledge Messrs. Steve Barson, Dale Cipra, Wallace Welder, and James Beck of Pratt & Whitney Rocketdyne for providing technical data for the Space Shuttle Main Engines.

[Visit the Resource Center for more SIMULIA customer papers](#)